Investigation of Regional Variation in Lunar Crater Morphometry from (Lunar Orbiter Laser Altimeter) LOLA Observations

by

Matthieu Jean Talpe

Submitted to the Department of Earth, Atmospheric and Planetary Sciences

in Partial Fulfillment of the Requirements for the Degree of

Bachelor of Science in Earth, Atmospheric and Planetary Sciences

at the Massachusetts Institute of Technology

May 24, 2011 [June 2011]

Author Signature redacted

Matthieu J. Talpe
Department of Earth, Atmospheric and Planetary Sciences
May 24, 2011

Certified by Signature redacted

Maria T. Zuber
Thesis Supervisor

Accepted by Signature redacted

Samuel Bowring
Chair, Committee on Undergraduate Program

Abstract

The advent of global Digital Elevation Models of the lunar surface, obtained from the Lunar Orbiter Laser Altimeter (LOLA), has allowed for a quantitative assessment of crater morphometry. 351 simple and complex craters in the Mare Serenitatis, far side highlands, near side highlands, and South Pole-Aitken basin are decomposed into 50 elevation profiles, from which key geometric crater properties are extracted. The geometric properties and their respective standard variation, such as height-to-diameter ratios, and average elevation profile are compared on a global level to investigate regional differences in terrain rheology and study the transition between the simple and complex crater regime. Furthermore, the relationship between known degradation mechanisms and crater morphometry is discussed, as well as the current state of quantitative methods to assess crater degradation. The resulting regional differences observed in crater morphometry are explained in the context of lunar geologic history. Finally, the addition of other crater geometric properties in future quantitative assessments will broaden the study of crater morphometry, and improvements to current methods are necessary to conclusively define degradation states in terms of quantitative factors.

Acknowledgment

First and foremost, I thank Professor Maria Zuber for her invaluable guidance as an academic and UROP advisor. The research opportunities and regular discussions have undoubtedly defined my academic experience while at MIT. I have a profound admiration for the wide array of her accomplishments.

Furthermore, I am indebted to graduate students Paul Richardson, Michael Sori, Frank Centilleno, and Grant Farmer for their widely sought after assistance and wise perspective. In four years at MIT, Erwan Mazarico, former MIT graduate student and current GSFC extraordinaire, has never failed to answer my countless questions, almost always within minutes. I thank Professor Richard Binzel for sitting down with me three and a half years ago, one cold Friday evening in January, to talk for nearly three hours about space exploration and many other interesting topics—both in English and French.

Finally, I am grateful to the camaraderie of the brothers of Phi Sigma Kappa, the unwavering support of my family on both sides of the Atlantic, and last but not least, the companionship of the one and only Holly Mathews. Without her, I would still be stuck in Girona's lonely train station.

Contents

I. Abstract 2
II. Acknowledgment 3
III. Contents 4
IV. List of Figures 5
V. List of Tables 6
VI. Introduction .....
1. Science Background 7
2. The Lunar Reconnaissance Orbiter (LRO) Mission 8
3. Past Research and Current Approach 9
VII. Methods .....
1. Laser Altimeter Technology 11
A. Instrument Design 12
B. Instrument Implementation 13
C. Science Products 15
2. Crater Morphometry Analysis 16
A. Crater Selection 16
B. Crater Profile Decomposition 17
C. Assessment of Crater Morphometry 18
D. Measurement Corrections 19
i. Imperfect Altimetry Interpolation 20
ii. Latitude-dependent Variance of East-West Distances 20
E. Case-study: Bessel Crater 21
VIII. Results .....
1. Crater Selection 25
2. Depth Values 27
3. Diameter Values 27
4. Wall Variation Values 28
IX. Analysis .....
1. Size-dependence of Crater Morphometry 29
A. Crater Regime Differentiation 29
B. Height-to-diameter Fitting 30
C. Simple-to-complex Transitions 32
2. Crater Degradation from Quantitative Comparison 34
X. Discussion .....
1. Regional Variation 36
2. Problematic Nature of Degradation Evaluation 37
XI. Conclusion 38
XII. Bibliography 41

List of Figures

1. Artist rendition of LRO 9
2. The four areas studied 10
3. LOLA schematic 12
4. 5-beam pulse schematic 13
5. 5-beam ground pattern 14
6. Near side highland crater selection 16
7. LROC images of Bessel crater 22
8. 25 diametrical profiles of Bessel Crater 22
9. Radial decomposition of Bessel crater 23
10. Global distribution of craters 24
11. Regional distribution of craters 24-25
12. Histogram of morphometry data 25
13. Boxplot of depth data 26
14. Boxplot of diameter data 27
15. Boxplot of vertical variation data 27
16. Fresh crater fitting 30
17. Regional comparison of fitting coefficients 31
18. Inflexions in height-to-diameter data 32
19. Pike's 1974 height-to-diameter data 33
20. Variability in crater profile comparison 34
21. Assessment of degradation states 38

List of Tables

1. LOLA design guidelines 12
2. LOLA laser specs 13
3. Characteristics of crater decomposition 19-20
4. Correction of Bessel morphometry measurements 24
5. Fresh crater fitting statistics 31
6. Transition diameters 33

Introduction

1. SCIENCE BACKGROUND

The Moon's intriguing shapes and colors have mesmerized countless generations of sky gazers. The lunar surface has also provided scientists with a unique opportunity to study planetary rheology and its associated surface processes. Indeed, the absence of atmosphere and lack of rapid surface degradation mechanisms, such as aqueous erosion, have preserved many of the Moon's surface features. The surface's diversity is best demonstrated by the variety of impacts craters, most of them being remnant from the solar system's heavy bombardment period. The craters' uneven geographic distribution and heterogeneous morphometries are remarkable testaments of the Moon's complex geologic history.

The study of crater morphometry is a central aspect of planetary geology. It not only provides insights on the solar system's dynamic early history, the nature of cratering mechanisms, but also, on subsurface rheology. Craters are indexed on the basis of attributes, which can include: floor depth, rim-to-rim diameter, central peak, rim height, peak complexity, ring frequency, bowl-shaped interior, flat floor, rim-wall terraces, etc (Melosh, 1989). Craters are classified on the basis of morphologic complexity, which increases with diameter size. Categories include simple craters, complex craters, proto-basins, and multi-ring basins, but crater cataloging can include even more classes (McGill, 1973).

Craters are the result of high-energy collisions between impactors, such as asteroids, and the targeted planet (de Pater, 2001). The last stage of the three-fold crater formation process, respectively known as the compression, excavation, and modification stages, is

composed of both short-term and long-term mechanisms that slowly but continually, smoothen the shape of the crater. On the moon, the dominant forces dictating crater degradation on long timescales are diffusion (creep transport, micrometeorite bombardment, etc) and viscous relaxation due local isostatic compensation (de Pater, 2001).

2. THE LUNAR RECONNAISSANCE ORBITER (LRO) MISSION

In addition to the inherent scientific appeal of the preserved lunar surface, the Moon has garnered the attention of recent space-faring ambitions. NASA has sought to prepare future lunar exploration and has funded unmanned research of the lunar environment. The Lunar Reconnaissance Orbiter (LRO), shown in Figure 1, is NASA's most recent lunar science spacecraft and carries a scientific payload of seven instruments (Smith, 2010b). Its space altimeter, the Lunar Orbiter Laser Altimeter (LOLA), has been mapping the Moon since September 2009 (Smith, 2010a). The near-continual activity of LOLA, and the radio tracking of the spacecraft have generated the topography data necessary to generate high-resolution global elevations map of the lunar surface. The collection of topography data is motivated by the expectation of finding reliable landing sites for future lunar exploration, but it also serves the planetary geology community. Indeed, the polar orbits have allowed for the completion of the first fully global coverage of the planet, uncovering previously unknown areas of the Moon, such as permanently shadowed regions at the poles. Moreover, despite similar exploration missions from the Indian and Japanese space agencies, LOLA-derived maps are unique because of the exceptionally dense spatial coverage and unprecedented reliability (Smith, 2010a).

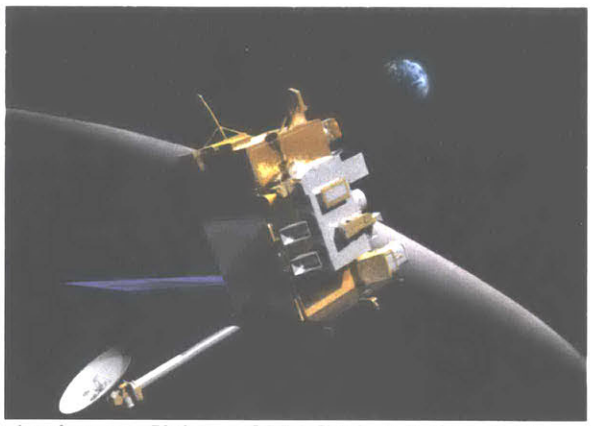

Figure 1: Artist rendition of NASA's LRO orbiting the Moon (http://lunar.gsfc.nasa.gov/).

3. PAST RESEARCH AND CURRENT APPROACH

Prior to the advent of Digital Elevation Models, elevations were determined through photogrammic techniques. Photogrammic techniques involved tedious calculations translating shadow lengths observed in images into elevation profiles from the knowledge of solar position at the moment of the image. As such, past lunar crater morphometry research was derived fom photogrammic calculations.

In this study, we benefit from the availability of high-resolution topography maps to design novel geomorphology measurement methods. The quantitative decomposition of each individual crater generates values for crater height, commonly referred to as depth, crater diameter, wall variation, coefficients for fourth-degree expansion, and an average crater profile. The data aggregated from 351 craters is used to examine and explain regional differences, and seek to infer information on the degradation states of lunar craters from the assessment of crater profiles.

The Mare Serenitatis, the South Pole-Aitken basin, and patches of the near side highlands and far side highlands are four regions of dissimilar geologic history whose craters are examined, as shown in Figure 2.

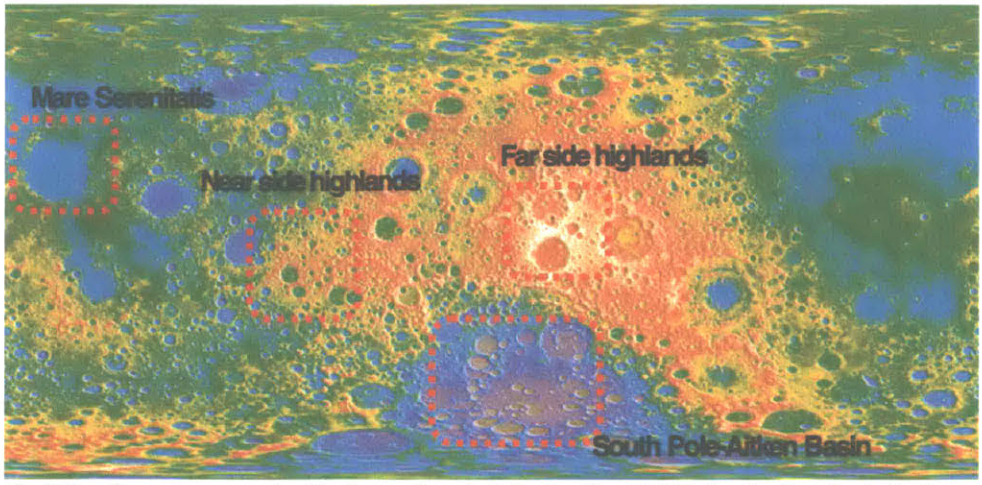

Figure 2: The four areas studied made visible in the LOLA-derived global map. The color gradient represents the wide range of lunar topography.

The Mare Serenatitis is a low-lying region of the lunar near side that has undergone significant re-surfacing processes. The highlands are some of the oldest areas of the Moon and characterize the higher altitude landscape. The SP-A basin is a unique topography feature: a 2,500-kilometer diameter and 8.2-kilometer deep basin, remnant of the largest impact in lunar history (Pieters, 2001).

METHODS

1. LASER ALTIMETER TECHNOLOGY

A detailed account of the design and performance of the LOLA instrument can be found in (Zuber, 2010) and (Smith, 2010b). Here we provide a brief summary for context.

A. INSTRUMENT DESIGN

The Lunar Orbiter Laser Altimeter (LOLA) is one of the six scientific instruments that comprise the payload NASA's Lunar Reconnaissance Orbiter (LRO). LOLA is a laser altimeter whose primary objective is to generate high-resolution maps of the lunar topography and surface roughness, slopes and reflectance at the laser wavelength (Smith, 2010b).

The instrument design is closely related to that of space altimeters that have successfully served on other planetary exploration missions. The Mars Orbiter Laser Altimeter (MOLA) collected over 600 million topography points of the Martian surface over its nine-year life and has been the inspiration for dozens of publications (Planetary Geodynamics). The NEAR Laser Rangefinder (NRL) provided novel precision altimetry measurements of the surface of asteroid 433 Eros (Cole, 1998). Finally, the MESSENGER Laser Altimeter (MLA) is an instrument aboard the MEercury Surface Space Environment, Geochemistry, and Ranging (MESSENGER) spacecraft, currently in its orbital mapping phase around Mercury. As an instrument on the first spacecraft to orbit Mercury, MLA is expected to provide a unique global dataset of the topography of the northern hemisphere of this planet. A common attribute of previous space-based laser altimeters is that they were single-beam profiling instruments. The LOLA instrument represents a technological advance to a multi-beam system.

Exploration ambitions to land spacecrafts on the Moon have highlighted the need for high-resolution lunar maps, thereby providing strict guidelines for LOLA, as described in Table 1.

Table 1: Design guidelines for LOLA's science results.

Design Parameter	*Value*
Slope accuracy in two directions	±1°, 10-m baseline
Elevation precision	± 0.1 m
Radial accuracy	< 1 m
Horizontal accuracy	< 50 m
Surface roughness	0.3 m
Geodetic grid accuracy	50 m (horizontal) < 1 m (vertical)

B. INSTRUMENT IMPLEMENTATION

Space altimeters consist of at least one laser transmitter, a receiver, and one or more detectors. A schematic of LOLA is shown in Figure 3. The passive radiator regulates the temperature of the instrument from the thermal stresses of the spacecraft environment.

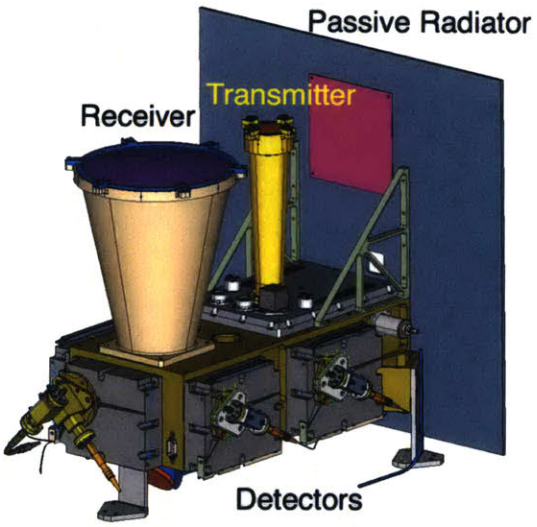

Figure 3: Schematic of LOLA instrument (http://lunar.gsfc.nasa.gov/lola/details.html). **The transmitters fires laser pulses and the receiver measures the properties of the returned pulses.**

The transmitter consists of two diode-pumped lasers, providing a redundant lasing source. The laser specifications are described in Table 2.

Table 2: LOLA laser specs.

Parameter	*Value*
Laser wavelength	1064.4 nm
Pulse energy	2.7 mJ (laser 1) 3.2 mJ (laser 2)
Pulse width	5 ns
Pulse rate	28 ± 0.1 Hz
Beam divergence before the DOE	100 ± 10 μrad
Beam separation after the DOE	500 ± 20 μrad

The Differential Optical Element (DOE) splits the pulse into five beams that are directed to the surface of the Moon, as illustrated in Figure 4. The five-beam pattern allows for a cross-section measurement of altimetry, quantifying local slope of the lunar surface (Smith, 2010b).

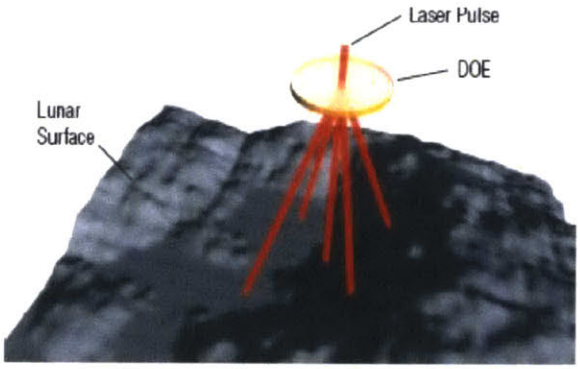

Figure 4: Schematic of 5-beam pulse implementation (http://lunar.gsfc.nasa.gov/lola/details.html). The DOE splits the laser pulse into five beams, permitting a novel assessment of lunar topography.

The footprint forms an X pattern. From the LRO orbital mapping altitude of 50 km above the lunar surface, each spot is approximately 5 meters in diameter and separated from one another by 10 meters, as shown in Figure 5.

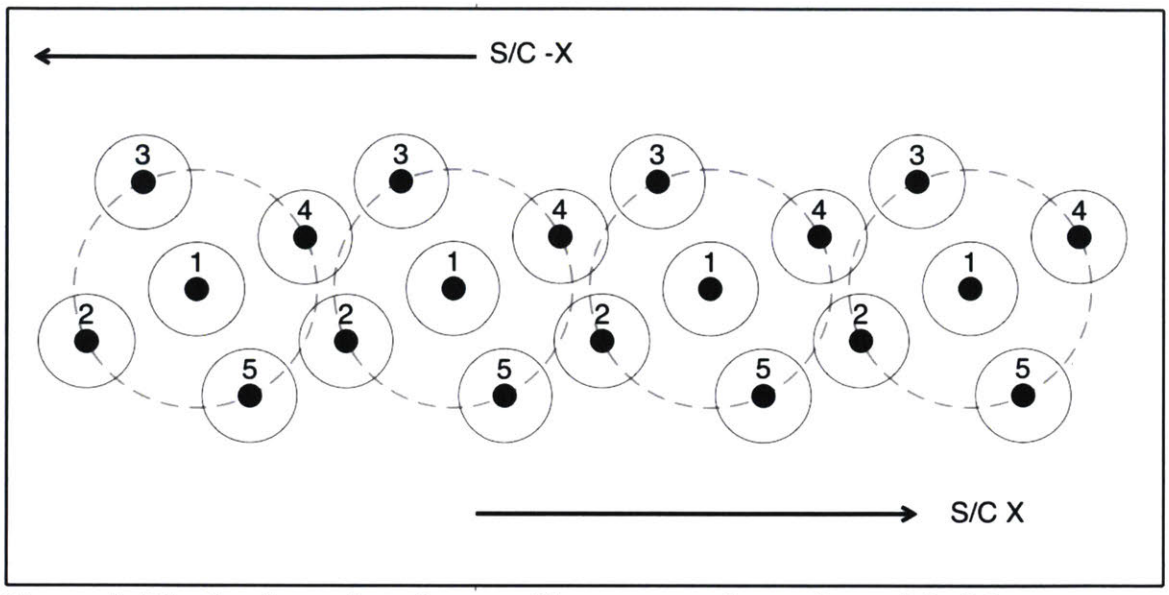

Figure 5: The five laser shots form an X pattern on the surface of the Moon (http://lunar.gsfc.nasa.gov/lola/details.html).

The receiver is a 14-cm diameter refractive telescope designed to focus the photons scattered from the surface of the Moon into a fiber optic bundle. The photons are then carried to the detectors. To minimize background noise, a dielectric fold mirror in the receiver and band-pass filter in the receivers only allow for radiation at the 1064-nm wavelength.

The LOLA detectors measure backscattered laser energy from the lunar surface. An oscillator measures the time of flight (TOF) of the outgoing pulse. Also measured are the returned energy and width of each pulse. Instrument biases are corrected in-flight by onboard computers. The three main biases are: the LOLA TOF to range bias, the internal instrument timing bias, and the pulse width and impulse response bias, all of which are described in greater detail in (Smith, 2010b). The distance D between LRO and the lunar surface is determined by:

$$D = \frac{c}{2} \times (T_d - T_t), \quad \textbf{(2)}$$

where T_d is the time stamp of the detected pulse, T_t the time stamp of the transmitted pulse, and c the speed of light. Precision Orbit Determination accomplished by analysis of the LRO Doppler tracking data provides the position of the spacecraft with respect to the center of mass of the Moon. The spacecraft position minus the range to the surface provides precise measurements of the planetary radius at each laser shot point. Topography is determined by subtracting a sphere of 1737.4 km from each radius measurement.

C. SCIENCE PRODUCTS

LRO's Lunar Ranging (LR) system provides the precise orbit determination measurements necessary to generate a lunar reference grid. LR is implemented jointly by LOLA's one-way laser ranging and the radio tracking from NASA's Deep Space Network (Zuber, 2010) A global coverage of altimetry measurements is made possible by LRO's polar orbits. LOLA's North-South profiling is densest the poles, while the spacing between lunar tracks is the largest at the equator.

The LOLA data packets are transmitted to the LOLA Science Operations Center computer, located at the Goddard Space Flight Center, in Greenbelt, MD. The Experiment Data Record, LOLA's raw data, is processed via range calibration and orbital processing. The resulting Reduced Data Records are converted in Gridded Data Records. A global interpolation allows for the creation of equi-rectangular map projections of the lunar topography, the Lunar Digital Elevation Models (LDEM). As of the completion of this thesis, the highest resolution LDEM used were LDEM_512, which are composed of 16 tiles of 60-m-per-pixel resolution. The vertical resolution was 10-cm, and the radial accuracy is approximately 1 m with respect to the center-of-mass coordinate system.

2. CRATER MORPHOMETRY ANALYSIS

The creation of global lunar DEM from LOLA's activity and LRO tracking allowed for specific measurement of individual crater morphometry. Each crater was modeled from a high-resolution DEM and algorithms dissected its geometric properties. The height, diameter, wall variation, and their specific statistical variation were computed to quantify crater morphometry.

A. CRATER SELECTION

The coordinates of the approximate centers of individual craters' are initially selected from regional maps of LDEM_64, as shown in Figure 6.

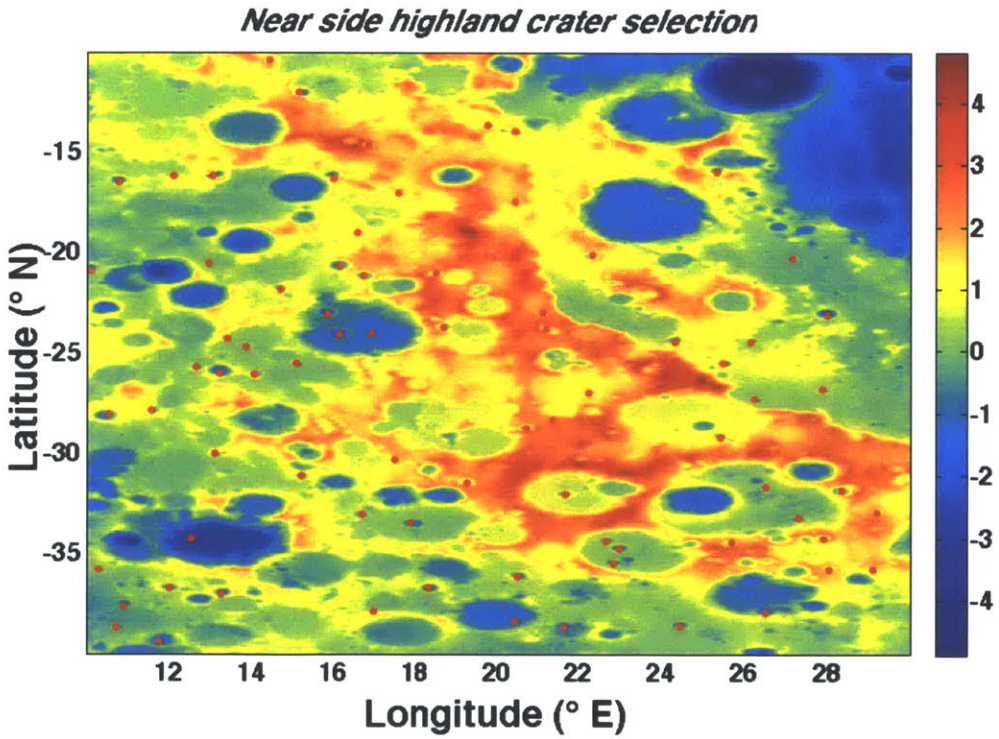

Figure 6: The red dots represent the craters examined in the near side highland region.

The craters examined were critically analyzed and those included in the study exhibited features expected of regular crater shapes: a continuously circular rim, ejecta deposits, regular crater walls, crater floor lower than the surrounding topography, etc.

Criteria that ruled out a crater from selection pertained to diameter and topographic details. Size was a factor because craters under 1-km diameter were deemed too small to provide enough reliable data points for the decomposition algorithms (described below), while craters over 30-km diameter were not of interest in this study. Furthermore, signs of secondary processes excluded certain craters. Examples of abnormal topography included over-printed craters and inter-crater deposition.

The subjective nature of crater selection was especially pronounced in the both patches of the highlands, where crater saturation is reached—impacts may only create a new crater by obliterating an existing one (Head, 2010). It is important to note that the purpose of this study was to quantify the nature of crater degradation, therefore we did not attempt to select ideally-shaped craters. We selected craters with a range of visual degradation states. However, we did seek to select according to the constraints described above to reduce error in the statistical assessment of the craters' morphometries.

A second round of analysis automatically isolated 2° by 2° areas from the LDEM_512 maps centered on each crater's approximate center.

A third round of analysis allowed the selection of the most relevant area of the LDEM_512 maps. Using the entire 2° by 2° inhibited fast crater analysis turnover given the large number of data points in each 2° by 2° LDEM_512 area.

B. CRATER PROFILE DECOMPOSITION

The fourth and final round of analysis was the decomposition of a crater into 25 diametrical profiles from its derived LDEM_512 map. An example of crater profile decomposition is illustrated with the Bessel crater in Part D.

Two input pixels locations were necessary to approximate the crater center and evaluate the radius desired. The radius selected was large enough to include altimetry measurements of the surrounding topography that wasn't affected by the crater impact. The first diametrical profile was horizontal and spanned from the center's horizontal pixel value to the radius' horizontal pixel value, without regard to the radius' vertical pixel value. The pixel length of the first diametrical remains the same for all 25 diametrical profiles. A rotational transformation of 7.2° (360/50) in the counter-clockwise direction allowed for the measurements of a second diametrical profile. The discrete nature of the grid data required bilinear interpolation to optimize the altimetry estimation of each pixel point. The same process of rotational transformation and bilinear interpolation was used to compute the altimetry of the remaining 23 diametrical profiles.

C. ASSESSMENT OF CRATER MORPHOMETRY

Data analysis was initiated once all the craters were decomposed into 25 diametrical profiles.

The first round of data analysis consisted of decomposing each diametrical profile into two radial profiles, resulting in 50 radial profiles per crater. The collection of the best 25 radial profiles was used to form an average crater profile (see D. i. for explanation of radial profile correction). The crater properties computed were crater depth, diameter, wall shape, and curvature, as shown in Table 3.

Table 3: Characteristics of crater decomposition.

Value measured	*Method*	
Crater Depth ***d***	Significance	The crater depth ***d*** is a basic measurement of crater morphometry. Crater depth ***d*** is the result of the excavation process of the impact balanced against the unloading of the shock wave that causes the target to rebound.
	Method	The crater depth was defined as the average depth of the collection of individual profiles. The depth of an individual radial profile was the elevation maximum, found at the summit of the crater wall, minus the elevation minimum.
Crater Diameter ***D***	Significance	The crater diameter is a basic measurement of crater morphometry. Crater diameter correlates with the kinetic energy of the impactor [10].
	Method	The crater diameter was twice the crater radius. The crater radius is the average radius of the collection of individual profiles. The radius of an individual profile is the distance between the elevation maximum and elevation minimum.
Crater Vertical Wall Variation ***W***	Significance	The value represents the variation of the crater wall.
	Method	The wall variation was evaluated from the comparison of each radial profile wall against the mean radial profile wall. The wall was defined as the set of altimetry data between the crater minimum and the crater maximum.

The depth, diameter, and wall variation values were characterized by standard deviation values. The standard deviation values originated from the contribution of all 50 radial profiles and served to examine the crater shape's asymmetry.

D. MEASUREMENT CORRECTIONS

i. Imperfect Altimetry Interpolation

A comparison between the Lunar Reconnaissance Orbiter Camera (LROC) image and the LDEM shows inconsistency in altimetry. LDEM exhibit periodic height irregularities, especially visible at the crater rim, as seen in Figure 6. The altimetry inconsistencies are due to the imperfect interpolation of LOLA data in a global digital elevation model. These data discrepancies are more pronounced in low coverage areas and, therefore, in regions closest to the equator where the LOLA tracks are spaced the farthest apart from each other. The correct data are the altimetry highs, which correspond to the exact LOLA tracks.

To remedy to the limitation of LDEM interpolation, the 25 profiles with the lowest heights were discarded. This approach strikes a balance between neglecting misleading data that throws off computations for all geometric property measurements and using data that rightfully quantifies crater asymmetry.

ii. Latitude-dependent Variance of East-West distances

The lunar DEM were equi-rectangular and, therefore, pixel distance did not vary with latitude. This posed a problem for regions away from the equator, where the projection distortion had no effect. However, the distortion only affected horizontal (West-East) distances. The pixel distance d_m in the vertical (North-South) direction remained constant and was calculated as follows,

$$d_m = \frac{2 \times \pi \times R_{Moon}}{N_d \times N_p} = 118.45 \ \frac{\text{m}}{\text{pix}}, \quad \textbf{(3)}$$

where R_{Moon} was taken to be the radius of the Moon (1,738.4 km), N_d the number of latitudinal degrees, and N_p the number of pixels per degree in the DEM (512).

To compensate for the projection distortion in the West-East directions, the horizontal pixel distance d_p^h was converted into d_m^h based on the following relationship,

$$\frac{d_m^h}{P_m^h} = \frac{d_p^h}{P_p^h}, \quad \textbf{(4)}$$

where P_m^h was the perimeter of the circle parallel to the equator at the latitude of the crater and P_p^h was the number of pixels in the West-East direction of the DEM. The perimeter P_m^h changed as a function of latitude according to the relationship,

$$P_m^h = 2 \times \pi \times R_{Moon} \times \cos(\alpha), \quad \textbf{(5)}$$

where α was the mean latitude of the crater. R_{Moon} was considered to be constant as the effect of the Moon's obliquity on the perimeter of the circle was negligible.

E. CASE STUDY: BESSEL CRATER

Bessel crater is located in the southern half of Mare Serenitatis (21°N, 17.9°E). Because of its diameter (~16-km diameter), the crater lies at the simple-to-complex boundary, where impacts are just energetic enough for elastic rebounding to create an uplifting of material at the center of the crater. As seen in Figure 7, Bessel exhibits signs of a flat floor and even accumulation of wall material, testament of wall linear creep degradation.

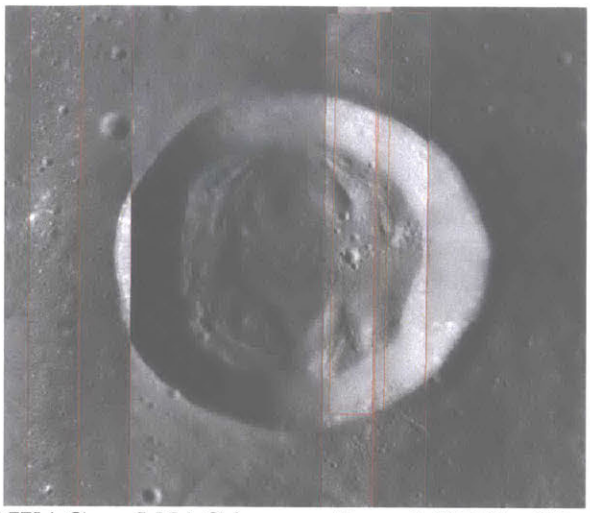

Figure 7: Mosaic of WAC and NAC images from LROC of Bessel crater.

Figure 8 shows the 25 altimetry diametric profiles overlaid over a higher resolution digital elevation model of Bessel.

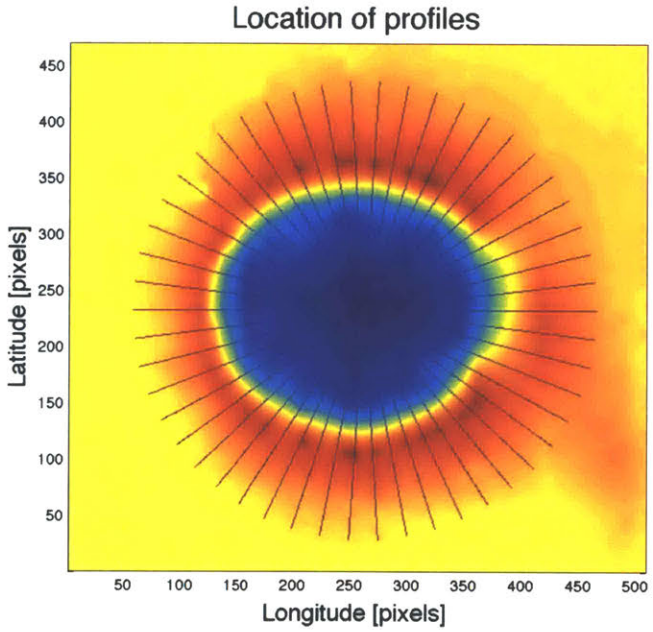

Figure 8. The 25 diametrical profiles of the Bessel crater.

The 25 diametric profiles were converted to 50 radial profiles that form the green plots in Figure 9. Each profile's maximum and minimum were marked by the black dots. The two blue marks are the resulting averaged minimums and maximums. The 50 radial profiles

formed an average profile, seen as the red profile in both plots. The wall variation was illustrated by the black vertical error bars located at regular intervals on the bottom plot of Figure 9.

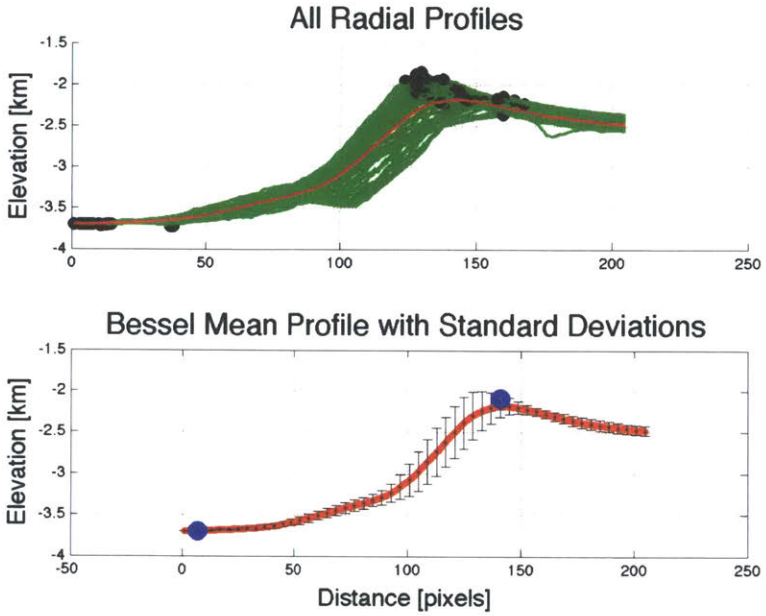

Figure 9: Bessel's radial decomposition.

Table 4: Morphometry of the Bessel crater before and after the interpolation correction.

Parameter	*Value before*	*Value after*
Height d [km]	1.612 ± 0.137	1.707 ± 0.0612
Diameter D [km]	16.622 ± 2.316	15.736 ± 0.884
Wall Variation W_c [km]	0.108 ± 0.094	0.0648 ± 0.0468

A comparison between past morphometry profiling were consistent with the method described above. Pike's 1976 tabulation of 484 lunar craters from Apollo-based Lunar Topography Orthomaps found that Bessel is 1.77-km deep and had a 15.50-km diameter (Pike, 1976). The interpolation correction described in D.i. improved the morphometry measurements and reduced the variation of all measurements.

RESULTS

1. CRATER SELECTION

A total of 351 medium-sized craters were selected to undergo the morphometry analysis described previously. A distribution displaying the global distance between each region examined is seen in Figure 10. A regional view allows one to see most individual craters in Figure 11.

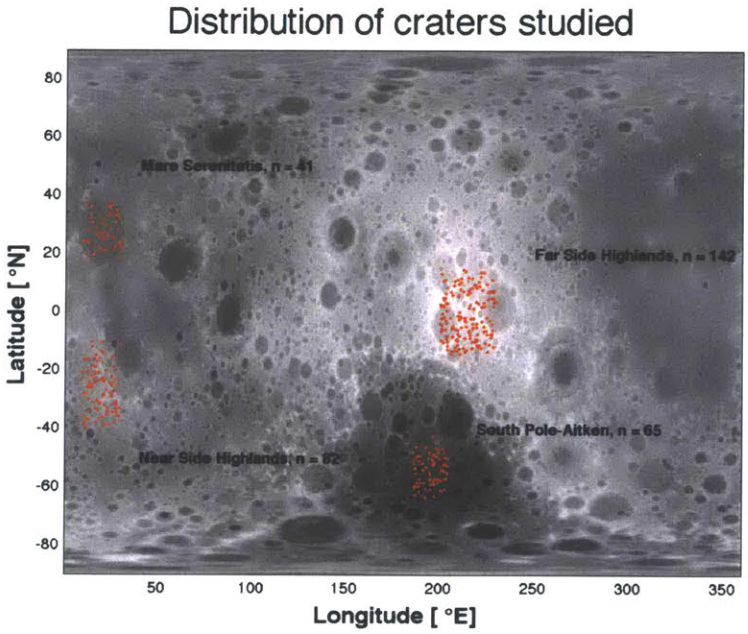

Figure 10: Global view of crater distribution on a 4 degree-per-pixel gray-scale LDEM. The lunar craters examined are marked by the red dots.

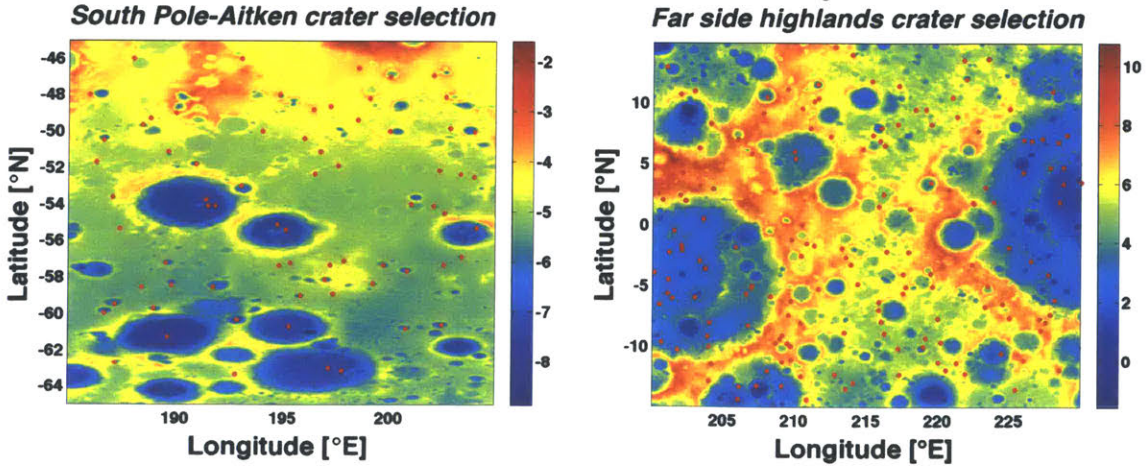

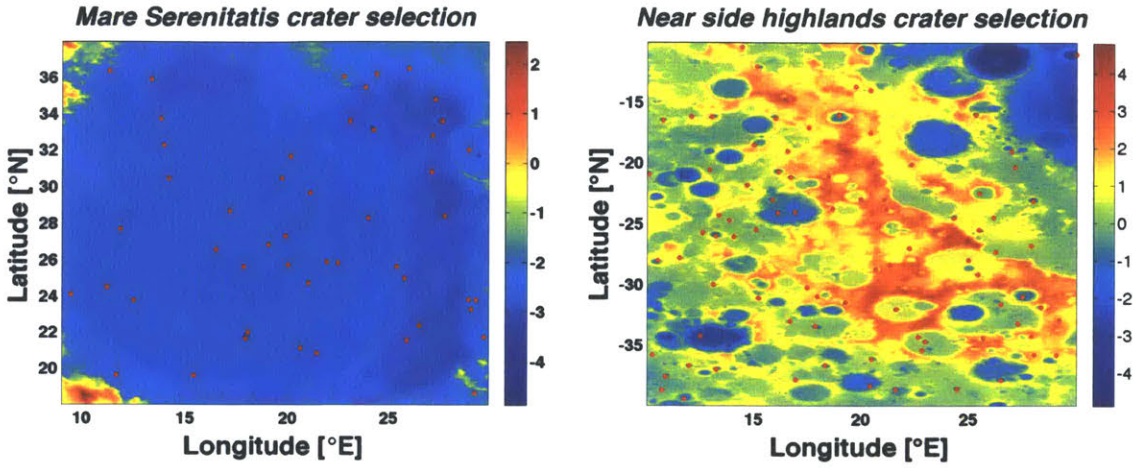

Figure 11: Regional view of crater distribution on 4 pix-per-degree color-scale LDEM. The lunar craters examined are marked by the red dots.

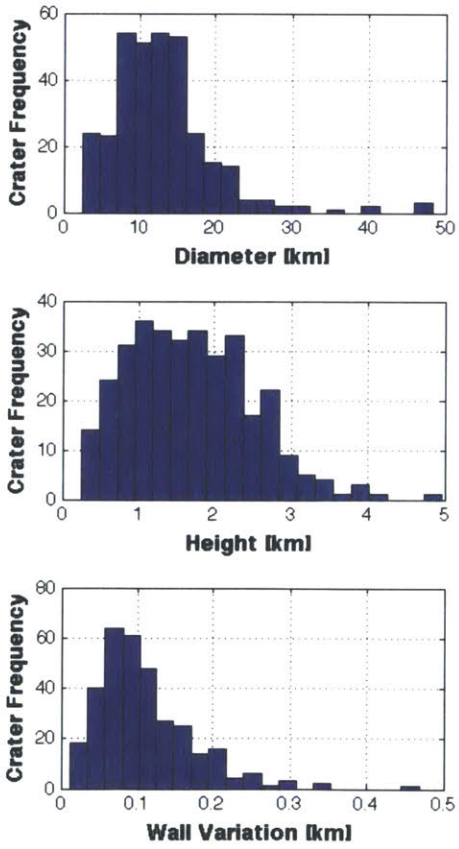

Figure 12: Histograms of basic crater morphometry. The distributions of geometric properties' values are centered on values of an average medium-sized lunar crater.

The morphometry analysis of individual crater yielded three principal geometric measurements, whose ranges are depicted in Figure 12, and their respective statistical standard deviations.

2. DEPTH VALUES

The depth of a crater is a basic geometric measurement of crater morphometry. The average. Depth values range from 0.253 to 4.963 kilometers with a mean value of 1.679 kilometer, as shown in Figure 4. The standard deviation and depth data show a weak correlation whereas the standard deviation to depth ratio data shows no correlation, as seen in Figure 5.

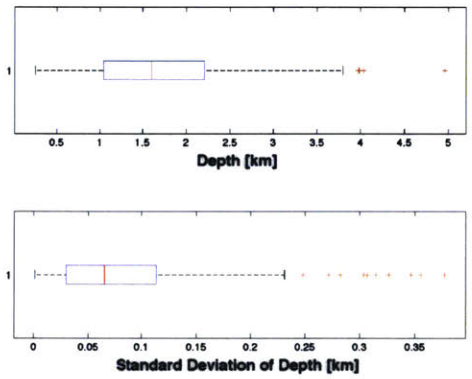

Figure 13: Global distribution of wall variation and standard deviation numerical values. A high number of outliers are seen at the large end of the standard deviation data.

3. DIAMETER VALUES

The diameter of a crater is a basic geometric measurement of crater morphometry. Diameter values range from 2.465 to 48.963 kilometers with a mean value of 12.939 kilometer, as shown in Figure 7.

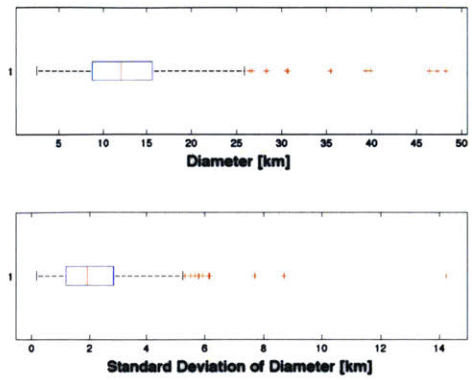

Figure 14: Global distribution of wall variation and standard deviation numerical values. A high number of outliers are seen at the large end of both the diameter and standard deviation data.

4. WALL VARIATION VALUES

The wall variation of a crater represents the average topography change as a function of radius orientation that occurs between the center of a crater and its rim. Wall variation values range from 0.0120 to 0.4681 kilometers with a mean value of 0.109 kilometer, as shown in Figure 15.

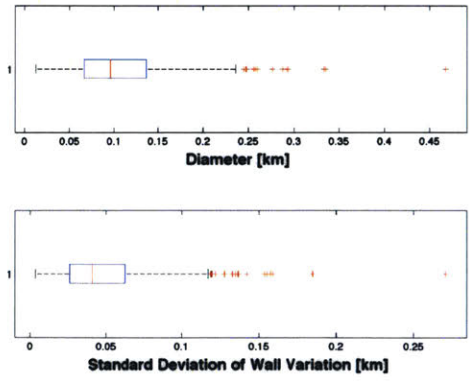

Figure 15: Global distribution of wall variation and standard deviation numerical values. A high number of outliers are observed at the large end of both the wall variation and standard deviation data.

Analysis

1. SIZE-DEPENDENCE OF CRATER MORPHOMETRY

The data aggregated from 351 craters by the method described above allowed for an examination of statistical relationships influencing crater morphometry. In order to facilitate the statistical comparison within the regions, craters were indexed in two different regimes: fresh or degraded and simple or complex. The first object of comparison is the height-to-diameter data. The second object of comparison is fresh crater fitting in order to examine the simple-to-complex transition.

A. CRATER REGIME DIFFERENTIATION

Fresh craters are defined as the twenty percent of the crater population that shows the highest height-to-diameter ratios, regardless of diameter size. Indeed, fresh craters typically possess a deeper floor and narrower diameters because of their young age, thereby translating to high height-do-diameter ratios. This selection allows for the creation of an upper-limit envelope in the height-to-diameter data.

Complex craters are first and foremost defined by specific features, such as central peak and flat floors. The features are observed in craters whose diameter extend beyond a certain diameter mark. Past lunar crater morphometry observations gathered by Melosh (Melosh, 1989), have established that craters between the diameters of 15 and 21 kilometers transition from a simple to complex regime, depending on the nature of the region. In this study, complex craters are designated as the craters to the right of the apparent morphological transition.

It is important to note that those selections are subjective tools to facilitate the differentiation of crater types in scatter plots, not a formal definition assigned to each individual crater.

B. HEIGHT-TO-DIAMETER FITTING

In this study, craters designated as fresh underwent a least-square logarithmic fit

$$h = b \cdot D + A, \qquad \textbf{(6)}$$

$$\ln(h) = e^{A} \cdot D^{b}, \qquad \textbf{(7)}$$

$$h = a \cdot D^{b}, \qquad \textbf{(8)}$$

where h is the height and D the diameter. The statistical correlation between the least-squares logarithmic fit and the height-to-diameter data was represented by R^2. Past observations have established an approximate fresh crater curve line applicable to all simple craters on the Moon, where,

$$h = D / 5. \qquad \textbf{(9)}$$

From the fresh crater curve line defined above, one can infer that the theoretically ideal coefficient values for a, b, and R^2 were respectively 0.2, 1, and 1. The computed values are summarized in Table 6 and compared on a regional basis in Figure 16.

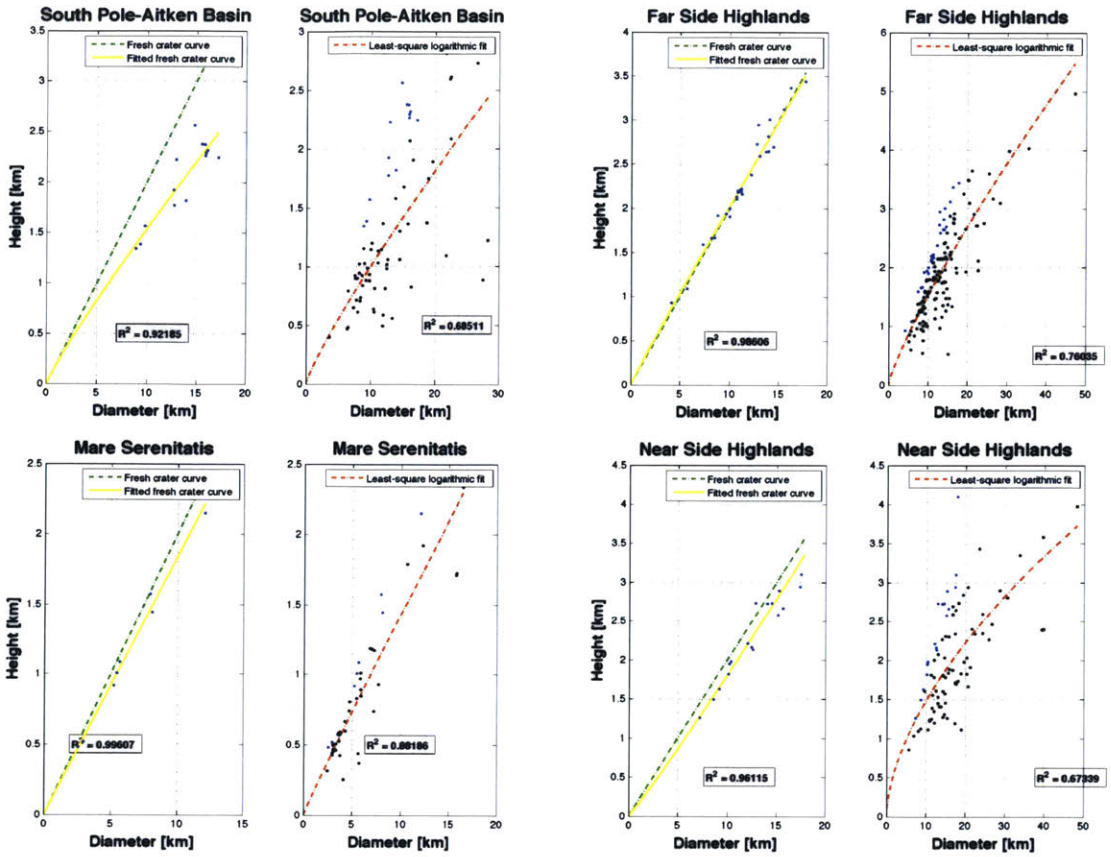

Figure 16: Fresh crater fitting. The blue dots are the crater points defined as fresh while the black dots are the remainder. The green line represents the established fresh crater curve line, the yellow line represents the fitted least-squared logarithmic fit applied to fresh craters, and the red line represents the least-squared logarithmic fit applied to all craters.

Table 5: Statistics of fresh crater fitting. The value *n* represents the number of craters, the coefficients *a* and *b* govern the least-square logarithmic fit while R^2 quantifies the correlation between the fit and the data.

REGION	ALL CRATERS			FRESH CRATERS		
	n	$d = a \cdot D^b$	R^2	***n***	$d = a \cdot D^b$	R^2
Near side highlar	88	a = 0.3875 b = 0.5840	0.6734	18	a = 0.1881 b = 0.9576	0.9422
Mare Serenitat	47	a = 0.1573 b = 0.9562	0.8819	9	a = 0.1846 b = 0.9987	0.9961
South Pole-Aitken	71	a = 0.1373 b = 0.8603	0.6851	14	a = 0.1952 b = 0.8953	0.9218
Far side highlan	145	a = 0.3875 b = 0.5840	0.7604	29	a = 0.1530 b = 1.0717	0.9612
ALL	351	a = 0.1992 b = 0.8236	0.7953	70	a = 0.1649 b = 1.0101	0.9749

The a and b coefficients and the correlation coefficients are compared on a regional level in Figure 2. Naturally, the fresh crater population coefficients demonstrate high correlation because the spread in height-to-diameter spread is smaller. Furthermore, they are inherently closer to the established fresh crater curve line.

Specific regional variations are observed. Of all regions, the craters in the Mare Serenitatis show the highest data correlation and the fitting coefficients are the closest to the theoretically established values for the fresh craters. Craters in the highlands demonstrate lower correlation, a sign of ample scattering in the height-to-diameter data. This effect is also demonstrated by the low b fitting coefficient in the highlands, which shows that the data is subject to a downward inflexion. In addition, the SPA fitting coefficient a, which governs the linear-like coefficient (assuming the exponential coefficient is close to 1), for the general population is noticeably smaller than others.

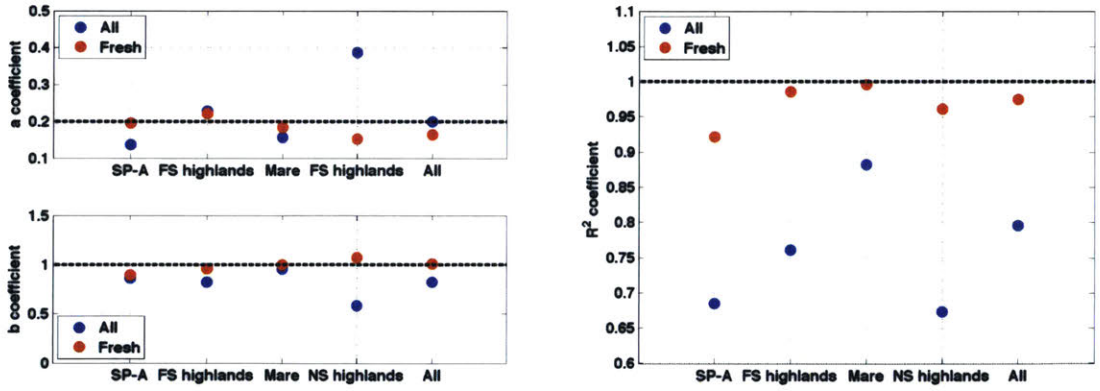

Figure 17: A regional comparison of fitting coefficients. The blue points represent the value obtained while fitting all the craters, while the red points represent the values obtained while fitting only the craters defined as fresh. The horizontal black dotted lines represent the ideal values.

C. SIMPLE-TO-COMPLEX TRANSITION

The morphological switch that occurs between bowl-shaped craters and more complex craters is referred to as the transition diameter D_t. That transition is made visible by the "knee" observed in a plot of fresh craters, as demonstrated in Figure 18.

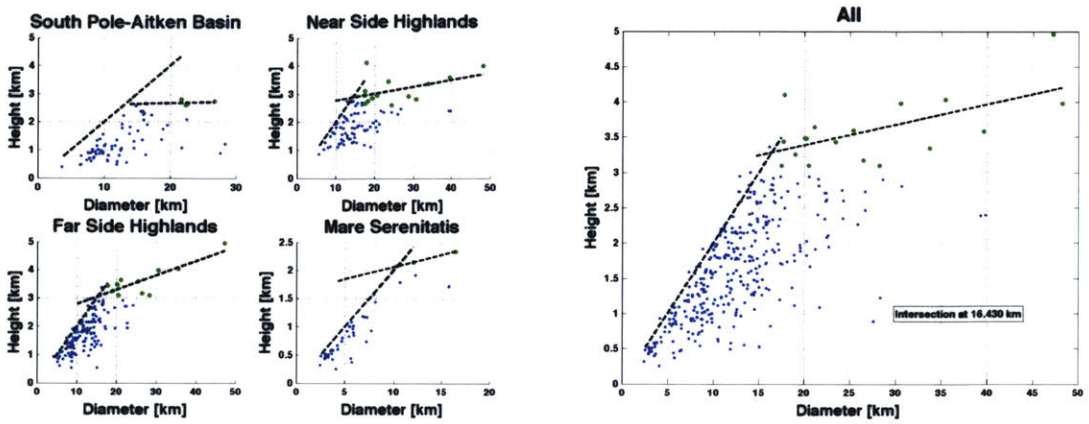

Figure 18: An inflexion in the height-to-diameter data appears clear for fresh craters. Fresh complex craters are marked as green dots.

The steeper line present in the left of each plot is the established envelope where the formula $d = D/5$ offers an approximate relationship between height and diameter for fresh simple craters. The shallower line at the right of each plot represents the linear fit of fresh complex craters. The intersection of the two lines defines the morphological transition D_t where impacts form craters features typical of complex craters, such as a central uplifting and hummocky floors. Transition diameters D_t for each region are tabulated in Table 1. The number of craters used for the "All" analysis is smaller than the sum of craters for each region because the criterion for complex craters was stricter, thereby making the resulting transition diameter D_t notably more reliable.

Table 6: Assessment of simple-to-complex transition diameters D_t. The value n is the number of craters used to compute the envelope delimiting fresh complex craters.

REGION	*n*	*D_t [km]*
Near side highlands	14	15.32
Mare Serenitatis	2	10.39
South Pole-Aitken basin	4	13.15
Far side highlands	12	14.37
ALL	**18**	**16.43**

The transition is the highest in the highlands, but the overall transition is made more reliable because the number of complex craters is largest. The transition diameter values correspond to previous studies that estimate the transition to approximately 16 kilometers (Melosh, 1989; Pike, 1974).

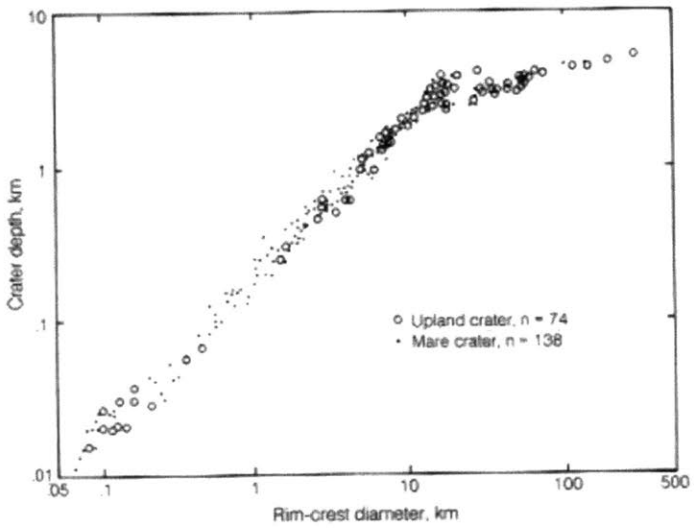

Figure 19: Height to diameter from the 1974 Pike study. The logarithmic scale accentuates the kink made visible by the morphological transition in lunar craters.

2. CRATER DEGRADATION FROM QUANTITATIVE COMPARISON

Long-term degradation mechanisms act by smoothening out crater profiles, but can also create features that result in sharp topographic signatures, such as wall slumping phenomenon, which create local rim-wall terraces. The occurrence of wall slumping translates into the deposit material at the bottom of the walls that accumulates over time. In ideal situations, those deposits reduce the wall angle in a quantitatively measurable way. Nevertheless, the high variability of crater profile made it impossible to design a robust method that could differentiate between smaller wall angles near the crater floors being due to topography variability or due to deposition. A qualitative assessment is therefore necessary to offer a reliable judgment for an individual crater. A similar

inability in quantitatively assessing wall terraces inhibits the design of a robust algorithm capable of any local change in curvature (the second derivative of elevation).

Another approach, one using the comparison of a theoretically fresh crater profile, was attempted. An elevation profile averaged from a normalized fresh crater population was used to provide an profile of references. Following appropriate distance scaling, the average crater profile was compared to each individual crater profile in the overall regional population However, average crater profiling did not yield conclusive linearity, as seen in Figure 20.

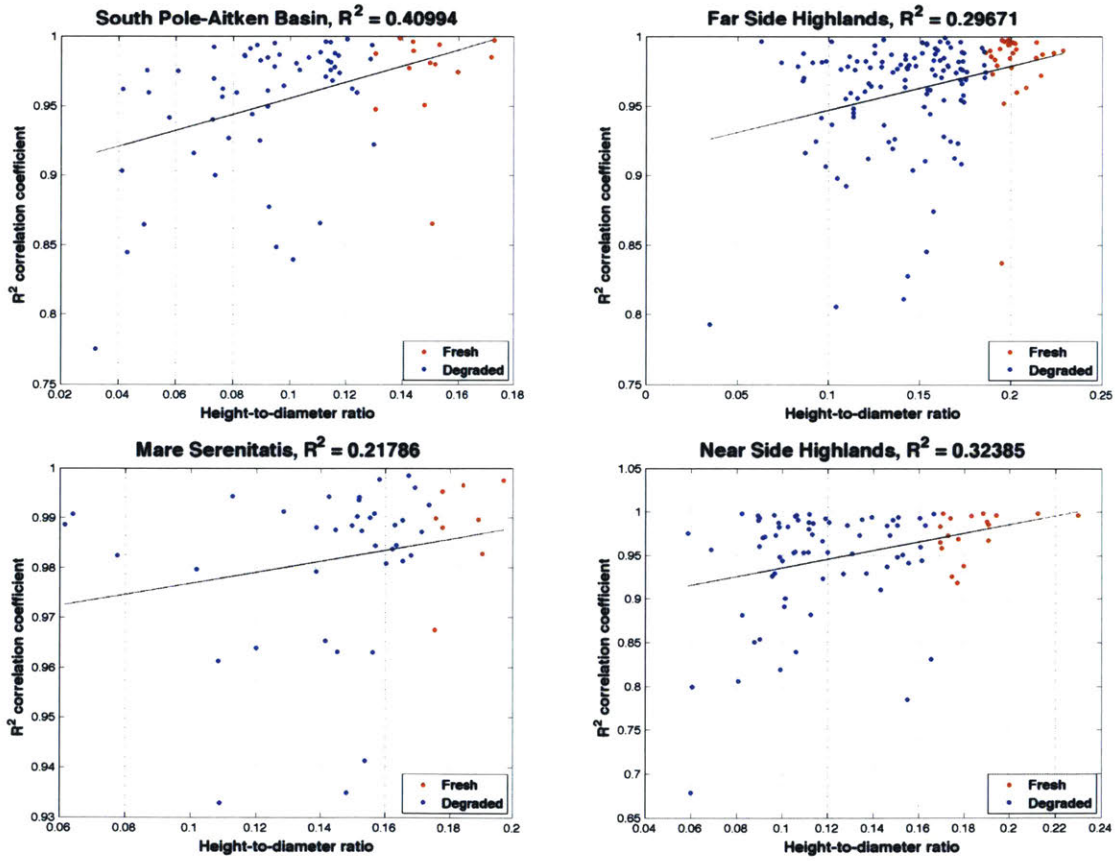

Figure 20: The variability in the comparison of crater profile.

Other preliminary fitting methods were attempted but proved to be redundant to information already acquired or insufficient. Fitting average profiles to polynomials or

Gaussian ultimately resembled height-to-diameter data. Indeed, average profiles are too smooth to show any kind of remarkable shape testament of degradation. The polynomial coefficients and/or Gaussian parameters are merely another way of inferring height-to-diameter.

Discussion

1. REGIONAL VARIATION

The height-to-diameter scatter plots highlight evident regional differences. Following the excavation stage of cratering impacts, three factors influence crater morphometry: surface gravity, target rheology, and the impactor itself. Surface gravity is assumed constant in all four regions, while this study does not seek to study the impactor. The measurement of height and diameters values for medium-sized craters allows for a specific assessment of the last influencing factor—target rheology. From the height and diameter data observed, three phenomenon warrant further explanation: the high proportion of fresh craters in the Mare, the large scatter observed in both patches of the highlands, and the low elevations of craters in the South Pole-Aitken basin.

First, craters in Mare Serenitatis exhibit high height-to-diameter ratios. This effect is quantitatively seen by the close correlation of logarithmic fit coefficients between the fresh crater population and the overall crater population in the Mare. Indeed, maria were formed from massive lava flooding. The flooding was trigged in the wake of colossal, lithosphere-weakening impacts that allowed for basaltic magma to surface. The flooding would have obliterated existing surface features. As the hot magma cooled in a geodetically stable shape, the previously marked surfaces would have been submerged into bare and flat surfaces. The magma flooding occurred early in the lunar history, but late enough to happen at the tail end of the Heavy Bombardment period. Furthermore, the surfacing of magma changed the surface composition of Maria, from igneous anorthosite, to basaltic rock, denser in nature. The timing of the magma flooding and the composition of the basalt material have allowed future Maria impact craters to remain preserved.

Second, craters in the highlands present a wide range of height-do-diameter ratios. The scatter illustrates the extensive crater degradation due to re-surfacing mechanisms from potential volcanic activity, linear diffusion creep, and ejecta from neighboring impacts, such as Orientale (Head, 2010).

Third, craters South Pole-Aikten Basin provide the most intriguing case of low height-to-diameter ratios. Because most of the lunar crust was excavated during the impact that formed the basin, the surface composition is not typical of the lunar surface (anorthosite) and presents local variation (Pieters, 2001). Magma infilling is not predominant, unlike in the maria (Pieters, 2001). Diffusion and its associate transport mechanisms are thought to be the major contributor to degradation in smaller craters (Smith, 1975). However, it is plausible that viscous elevation could explain the shift in height-to-diameter data in the South Pole-Aitken Basin, although viscous relaxation is generally considered to only affect longer wavelength features. But the excavation of several kilometers of lunar crust has possibly rendered the remaining crust warmer, rendering the South Pole-Aitken's underlying viscosity higher. Those conditions accelerate viscous relaxation, thereby smoothening out geological features (Hall, 1981). The resulting effects include smaller crater depths for a given diamter.

2. PROBLEMATICE NATURE OF DEGRADATION EVALUATION

The limitations of quantitative degradation assessment highlighted above reflect the problematic nature of excessive quantification when qualitative examination provides a more reliable assessment. It appears clear from known degradation mechanisms that as craters age, they become shallower, as illustrated in Figure 21.

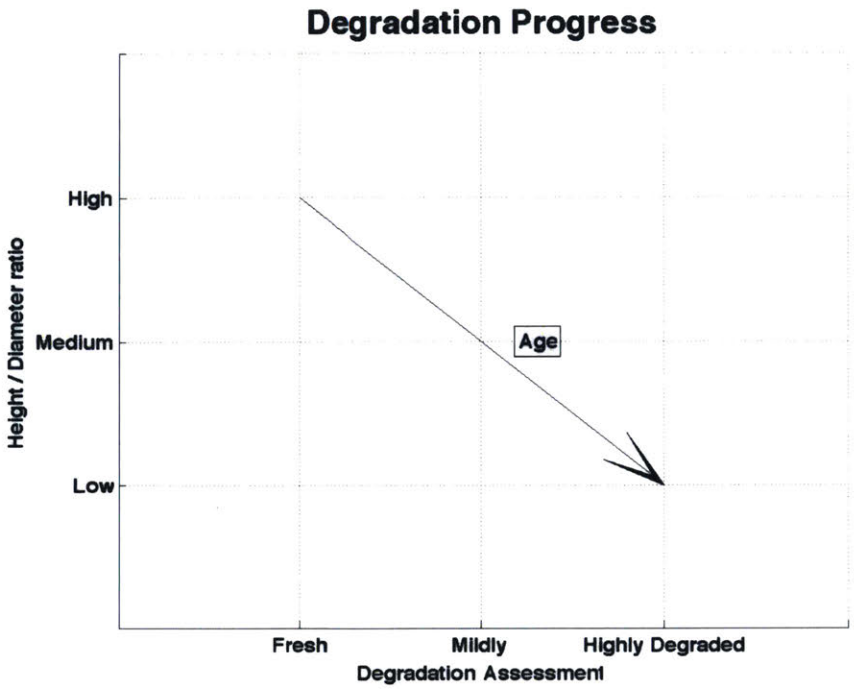

Figure 21: Relationship between degradation assessment and height-to-diameter ratio.

The aim of a quantitative assessment of degradation is essentially similar to being able to consistently assign a measurable quantity to degradation. However, computing crater shape, calculating degradation angle within the crater interior, detecting of complex crate feature incorporated into current morphometry-measurement algorithms, do not consistently function as a proper way of quantifying degradation.

One possible solution is to calculate erosional rates by estimating the volume of infilling. Such a volume could be computed by comparing the current profile of a crater, its simulated fresh profile, and integrating the difference in elevation (assuming it is circular) and, using Pappus's Centroid theorem, evaluate the corresponding volume. From an estimated crater age, one could then find an erosional rate. Such a method was used by Craddock and Howard to examine the type of material in various regions (Craddock, 1999).

Conclusion

This study produced notable facts of two different nature: one pertaining to the nature of Digital Elevation Model morphometry characterization and one pertaining to the nature of the results.

Past morphometry research utilized photogrammic measurements to determine crater geometry. The high-resolution digital elevation models generated from LOLA have opened the door to a novel approach to crater morphometry assessment. The methods greatly enhance the scope of crater assessment on a global scale while providing robust measurements. Future development to the algorithm-based method offers the promise of a quick and reliable characterization of multiple crater geometric properties and in the implementation of degradation quantification.

Quantitative (DEM-based) methods elaborated in this study to characterize degradation states of medium-sized craters are insufficient in drawing sound conclusions. The task of characterizing degradation is inherently opposed to the attempt at characterizing degradation with automatic algorithms. Indeed, the high variability in the topographical signature of denudation features requires a careful, case-by-case study of craters and/or more sophisticated methods that are not redundant to height-to-diameter measurements. However, Craddock and Howard's method of evaluating erosional rates offers a promising alternative to quantifying degradation.

The calculated crater geometric properties and their statistical variation of all craters in the four different areas show regional differences that highlight the subsurface rheology dissimilarities. The low number of degraded craters and high correlation of the crater population of Mare Serenitatis is a testament of maria's unique geologic history.

Similarly, many craters in the highlands demonstrate highly degraded states. Crater density is much higher in the highlands where crater saturation is reached (Head, 2010). The South Pole-Aitken basin contains a high crater density due to its old age, but also exhibits signs of the smooth plains infilling of larger craters and a notable regional lower height-to-diameter possibly explained by higher subsurface viscosity.

Bibliography

De Pater, I. and J. J. Lissauer (2001), *Planetary Sciences*, Cambridge University Press, Cambridge, U.K.

Cole, T. D. (1998), NEAR Laser Rangefinder: a tool for the mapping and topologic study of asteroid 433 Eros. *John Hopkins APL Technical Digest*, *19,* 142-157.

Craddock, R. A., and A. D. Howard (1999), Simulated degradation of lunar impact craters and a new method for age dating farside mare deposits, *Journal of Geophysical Research*, *105*, 20,387-20,401.

Hall, J. L, S. C. Solomon, and J. W. Head III (1981), Lunar Floor-Fractured Craters: Evidence for Viscous Relaxation of Crater Topography, *Journal of Geophysical Research*, *86*, 9537-9552.

Head, J. W. III, et. al. (2010), Global Distribution of Large Lunar Craters: Implications for Resurfacing and Impactor Populations, *Science*, *329*, doi: 10.1126/science.1195050.

McGill, G. E. (1974), Morphology of Lunar Craters: A Test of Lunar Erosional Models, *Icarus*, *121*, 437-447.

Melosh, H. J (1989), *Impact Cratering: A Geologic Process*, Oxford University Press, New York.

Pieters, C. M. (2001), Rock types of South Pole-Aitken basin and extent of basaltic volcanism, *Journal of Geophysical Research*, *106*, 28,001-28,022.

Pike, R. J. (1974), Depth/diameter relations of fresh lunar craters: Revision from spacecraft data, *Geophysical Research Letters*, *1*, 291–294.

Pike, R. J. (1976), Crater Dimensions from Apollo Data and Supplemental Sources. *The Moon*, *15*, 463-477.

Planetary Geodynamics, MOLA Shot Counter. Accessed March 21, 2011. <http://sebago.mit.edu/shots/>

Smith, E. I. (1976), Comparisons of the Crater Morphology-Size Relationship for Mars, Moon, and Mercury, *Icarus*, *28*, 543-550.

Smith, D. E., M. T. Zuber, et. al. (2010a), Initial Observations from the Lunar Orbiter Laser Altimeter (LOLA), *Geophysical Research Letters*, *37*, L18204, doi:10.1029/2010GL043751.

Smith, D. E., M. T. Zuber, et. al. (2010b), The Lunar Orbiter Laser Altimeter Investigation on the Lunar Reconnaissance Orbiter Mission, *Space Sci Rev*, *150*, 209-241, doi: 10.1007/s.11214-009-9512-y.

Whitehead, R. A. F., J. B. Garving, and J. G. Spray (2010), The effects of crater degradation and target differences on the morphologies of Martian complex craters, *Geologic Society of America Special Papers*, *465*, 67-80.

Zuber, M. T., D. E. Smith, et. al. (1994), The Shape and Internal Structure of the Moon from the Clementine Mission, *Science*, *266*, 1839-1843.

Zuber, M. T., D. E. Smith, et. al. (2010), The Lunar Reconnaissance Orbiter Laser Ranging Investigation, *Space Sci Rev*, *150*, 63-80, doi: 10.1007/s11214-009-99511-z.